Separation and Purification Technology 382 (2026) 136139

Contents lists available at ScienceDirect

Separation and Purification Technology

journal homepage: www.elsevier.com/locate/seppur

Alkyl-chain engineering of organonickel complexes advances interfacial solar evaporators for highly efficient seawater and wastewater purification

Joanna S. Lin [a], Pei-Yu Chen [a], Chen-Yang Hsu [a], Chen-Chieh Ni [a], Xinggui Gu [b], Jen-Shyang Ni [a,c,*]

[a] *Department of Chemical and Materials Engineering, National Kaohsiung University of Science and Technology (NKUST), Kaohsiung 807618, Taiwan*
[b] *Beijing Advanced Innovation Center for Soft Matter Science and Engineering, State Key Laboratory of Chemical Resource Engineering, College of Materials Science and Engineering, Beijing University of Chemical Technology, Beijing 100029, China*
[c] *Photo-sensitive Material Advanced Research and Technology Center (Photo-SMART), NKUST, Kaohsiung 807618, Taiwan*

ARTICLE INFO

Keywords:
Photothermal
Janus
Desalination
Solar-steam generation
SSG
NIR-II
IVCT

ABSTRACT

Solar-driven interfacial evaporation (SDIE) has emerged as a promising approach for sustainable water purification; however, its performance remains dependent on the design of efficient and tunable photothermal materials. In this work, alkyl chain-modified organonickel bis(dithiolene) complexes were developed and subsequently integrated onto filter paper substrates to create high-performance solar interfacial evaporators. By systematically varying the alkyl chain length, we demonstrate precise control over the complex's photothermal properties, molecular packing, and surface hydrophobicity on paper fibers. Specifically, the complex substituted with the long n-hexadecyl chain and possessing larger dihedral angles between dithiolene and thiophene units triggers intramolecular motion-induced photothermy, resulting in broadband solar absorption and efficient thermal localization. Under 1 sun irradiation, the SDIE device achieved a high evaporation rate of 1.72 ± 0.09 kg m^{-2} h^{-1}, corresponding to a solar-to-vapor efficiency of 98.48 ± 3.27%. This high efficiency, approaching and potentially exceeding the theoretical limit for 2D evaporators, is attributed to the light-trapping effect enabled by the filter paper's porous structure. Structural and spectroscopic analyses confirm the stable physical adsorption of the complexes on the filter paper fiber network, while cycling tests demonstrate excellent durability and desalination performance. This study highlights the potential of molecular-scale alkyl engineering for the development of tailored organometallic photothermal agents, providing a scalable platform for solar-driven water purification.

1. Introduction

Water scarcity is a serious global issue that not only affects ecosystems and human health but can also trigger food and economic crises. The United Nations proposed including "clean water and sanitation" as one of the Sustainable Development Goals (SDGs). To address the issue of water purification, various desalination techniques, including reverse osmosis, electrodialysis, mechanical vapor compression, and multi-stage flash distillation, have been developed to convert saline and brackish water into potable water. [1–3] However, these methods often involve high energy consumption, significant installation and maintenance costs, and environmental impacts. In contrast, solar-driven interfacial evaporation (SDIE) systems leverage clean solar energy to locally heat water at the water-air interface, thereby efficiently producing water vapor while minimizing thermal losses. [4,5] As expected, they not only exhibit high solar-to-vapor conversion efficiency, even exceeding 100% for 3D-designed devices, [6,7] but can also be manufactured in a large-scale, low-cost, and environmentally friendly manner. [8] In recent years, the SDIE technology has thus emerged as a promising alternative for sustainable and efficient water purification.

The critical component of the SDIE system is the photothermal conversion material (PTCM), which determines the efficiency of solar-to-thermal energy conversion. [9] To date, extensive research has focused on carbon-based materials [10], plasmonic nanoparticles [11,12], aerogels [13], metal-organic frameworks [14–16], semiconductors [17–19], semiconducting polymers [20], and organic small

---

[*] Corresponding author at: Department of Chemical and Materials Engineering, National Kaohsiung University of Science and Technology (NKUST), Kaohsiung 807618, Taiwan
E-mail address: jsni@nkust.edu.tw (J.-S. Ni).

https://doi.org/10.1016/j.seppur.2025.136139
Received 28 September 2025; Received in revised form 12 November 2025; Accepted 17 November 2025

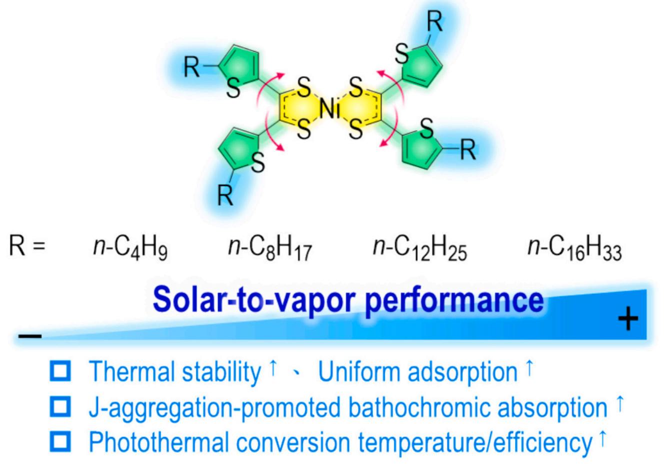

Scheme 1. The design strategy of alkyl-chain engineering on organonickel bis (dithiolene) complexes.

molecules. [21] Among the emerging candidate materials (Table S1), organonickel bis(dithiolene) complexes have recently attracted interest as advanced photothermal agents due to their intense and tunable absorption in the near-infrared (NIR) region, strong electronic delocalization, high thermal and chemical stability, and excellent photostability. [22] These characteristics originate from their square-planar conjugated structures and intervalence charge transfer (IVCT) transitions, [23] which enable them to form H- or J-aggregates on water transport substrates, such as paper and foam. [24] Interestingly, interfacial solar evaporators based on such H−/J-aggregation can achieve highly efficient sunlight harvesting from the visible to NIR region, making them particularly suitable for SDIE applications under solar irradiation. [24,25] Therefore, it remains a valuable approach to modify the molecular structures of these complexes in SDIE technology to optimize their photothermal properties. In particular, the role of alkyl chain substituents on the dithiolene ligands may provide a worthy avenue for exploring the relationship between molecular structure and solar-to-vapor performance.

Alkyl-chain engineering is a popular strategy to directly modify a range of chemical, physical, and even photophysical properties, including solubility, aggregation behavior, molecular hydrophilicity, thermal conductivity, and electronic delocalization. [26–28] In addition, the long alkyl chain in the donor-acceptor backbone can provide sufficient intermolecular space for the excited-state intramolecular motion in aggregates, allowing excited molecules to relax their molecular configuration back to the ground state through nonradiative energy-release pathways. [29] That is, this intramolecular motion-induced photothermy (iMIPT) phenomenon utilizes the nonradiative decay process of the material to efficiently convert light into thermal energy, further enhancing the photothermal conversion efficiency of PTCMs. [30,31] On the other hand, the terminal alkyl chain of conjugation materials can also effectively modulate the molecular orientation, [32,33] enhance the intermolecular interaction in aggregates, and promote their uniform dispersion and adsorption on porous matrices, facilitating the construction of excellent interfacial solar evaporators. As a result, introducing alkyl chains into the molecular structure of PTCMs would provide an opportunity to improve the efficiency of solar energy-to-steam conversion.

In this study, we investigate a series of organonickel bis(dithiolene) complexes with systematically varying alkyl chain lengths to evaluate their effects on photothermal behavior and overall evaporation performance in the SDIE platform (Scheme 1). Along with the alkyl chain length of complexes extending from n-butyl to n-hexadecyl, the decomposition temperature at 5% weight loss was improved from 182 to 322 °C due to increased molecular weights. Among them, the long n-hexadecyl chain substituted complex (NiTh16) can be dispersedly adsorbed onto filter paper to form a solar interfacial evaporator with a broad, continuous absorption band and a higher photothermal conversion temperature, reaching 185 °C within 20 s under 1064 nm laser irradiation. Moreover, the hydrophobic alkyl chain-modified paper fibers and pores can inhibit salt accumulation, thereby achieving effective salt removal and enhancing the efficiency of solar energy conversion into steam. Under one-sun radiation, the water evaporation rate ($\dot{m}$) of seawater can be as high as 1.67 ± 0.06 kg m^{-2} h^{-1}, with an efficiency of 95.0%. This performance is quite close to the theoretical value of the two-dimensional SDIE system [24], which is attributed to the stability, durability, and salt tolerance of the organonickel complex-adsorbed evaporator. For contaminated aqueous solutions, the $\dot{m}$ value can also reach 1.65–1.69 kg m^{-2} h^{-1}. Through systematic alkyl-chain modification on complexes, the relationship between the molecular structure, photothermal property, and STIL morphology is explained in depth, and the impact on the SDIE system is further demonstrated. All in all, this investigation highlights a molecular design strategy for optimizing organonickel molecules through alkyl chain engineering, advancing highly efficient solar evaporation technologies.

2. Materials and methods

2.1. Chemicals and instrumentation

Chemicals were purchased from Acros Organics and Alfa Aesar and used directly without further purification. ^1H and ^{13}C nuclear magnetic resonance (NMR) and high-resolution mass (HRMS) spectra were recorded on a Varian VNMRS 600 MHz spectrometer, using $CDCl_3$ as the solvent, and an Autoflex Speed Bruker, operated in MALDI-TOF mode, respectively. The thermogravimetric analysis (TGA) was recorded on the Mettler-Toledo spectrometer, with a heating rate of 20 °C min^{-1}. Fourier-transform infrared spectroscopy (FTIR) was measured with a PerkinElmer Spectrum 3 FT-IR spectrometer. UV–vis-NIR absorption spectrum was recorded on a ProTrusTech spectrometer (Taiwan) with an Avantes' SensLine and MRID. The X-ray photoelectron spectrometer (XPS) was recorded on a Thermo K-Alpha. The contact angle was measured with the OSA 60, NBSI. The scanning electron microscope (SEM) and inductively coupled plasma optical emission spectrometry (ICP-OES) were recorded on the JSM-5610 and iCAP 7000 Series, respectively.

2.2. Synthesis of neutral organonickel bisdithiolene complexes

1,2-Bis(5-alkylthiophen-2-yl)ethane-1,2-dione (2.0 equiv.) and phosphorus pentasulfide (4.7 equiv.) are dissolved in 1,3-dimethyl-2-imidazo-lidinone (0.1 M) and then heated at 95 °C for 10 h. A solution of nickel chloride hexahydrate (1.0 equiv.) in distilled water (0.4 M) is added to the reaction mixtures and further heated at 90 °C for 2 h. After cooling to room temperature, the solution is poured into distilled water and extracted with dichloromethane (CH_2Cl_2) three times. The combined organic fractions are dried over anhydrous magnesium sulfate, concentrated, and purified by column chromatography on silica gel using the CH_2Cl_2/hexanes mixture (1/4, v/v, R_f, 0.8) as the eluent, yielding a dark-green solid, NiThR derivatives. The details of the relevant chemical structure identification results are described in the Supporting information.

2.3. Fabrication of SDIE device

The 3.0 mg of NiThR derivative was dissolved in dichloromethane and added dropwise onto an 18 mm diameter filter paper (FP) for adsorption. The NiThR-adsorbed FP (NiThR@FP) was then dried at 40 °C for one day to prepare the solar-thermal conversion interface layers (STILs), noted as NiTh4@FP, NiTh8@FP, NiTh12@FP, and NiTh16@FP, respectively. As above, NiTh16 with different loading

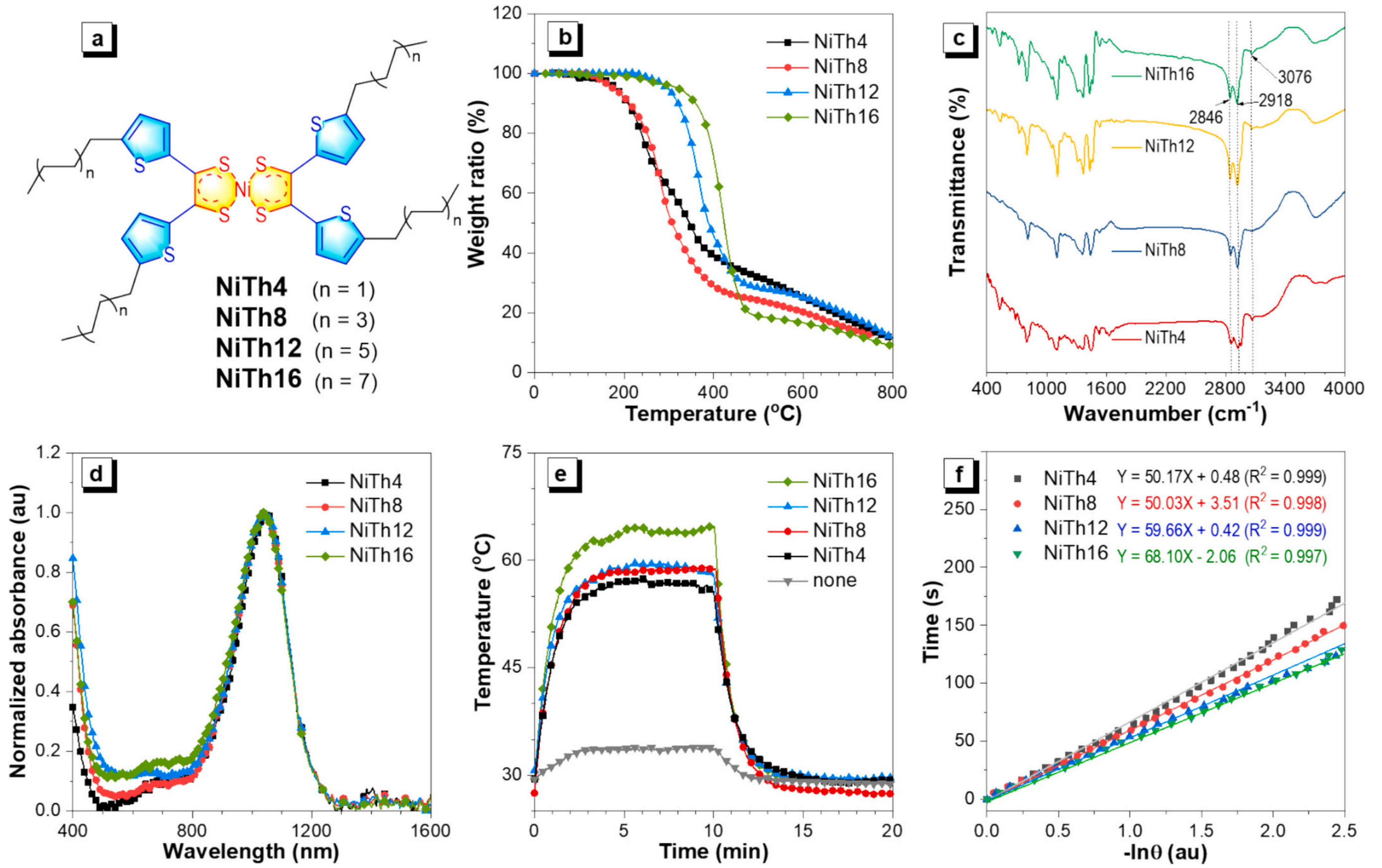

Fig. 1. Photophysical and photothermal properties of NiThR derivatives. (a) Chemical structures, (b) TGA spectra, (c) FTIR spectra, (d) normalized UV–vis-NIR absorption spectra in dichloromethane (10 μM), (e) time-dependent temperature changes in chlorobenzene (10 μM) under 1064 nm irradiation (1 W cm^{-1}), (f) The plot of irradiation time versus –ln(θ). θ is the driving-force temperature. The inset shows the fitting equation, where the slope indicates the system time constant (τ_s).

amounts (1.50, 2.25, 3.75, 4.50 mg) on filter papers with a diameter of 25 mm was also prepared. A cylinder of Melamine sponge, with a diameter of 45 mm and a thickness of 27 mm, served as both thermal insulation and support for STILs. The SDIE system, containing NiThR derivatives-adsorbed filter paper and sponge insulation, was placed in a 50 mL beaker filled with deionized water, seawater, and polluted water, respectively. It was then irradiated with different solar powers (0.5, 1.0, 1.5, 2.0, and 3.0 suns) and concurrently recorded water loss.

3. Results and discussion

3.1. Optical and photothermal properties of NiThR derivatives

As shown in the synthetic routes (Scheme S1), the organonickel complexes based on bis(dithiolene) ligands with different alkyl chain lengths (Fig. 1a) were synthesized via a one-pot coordination method, which is a relatively facile preparation compared with conventional organic STCMs. Herein, the organonickel complexes substituted with *n*-butyl-, *n*-octyl-, *n*-dodecyl-, and *n*-hexadecyl-chains are named NiTh4, NiTh8, NiTh12, and NiTh16, respectively. Their molecular identifications, including ^{1}H and ^{13}C NMR and HRMS spectra, are provided in the Supporting Information. The thermogravimetric analysis (TGA; Fig. 1b) shows that complexes tying long alkyl chains have higher thermal decomposition temperatures (297.7 °C for NiTh12 and 321.7 °C for NiTh16) than those with short chains (182.3 °C for NiTh4 and 175.0 °C for NiTh8), with 5% weight loss. The main substituent decomposition process is divided into three distinct steps (Figs. S1-S4): (i) Alkyl chains pyrolysis: The pyrolysis temperature of the alkyl chains generally increases with molecular weight: NiTh4 (269 °C), NiTh8 (243 °C), NiTh12 (396 °C), and NiTh16 (~435 °C). This step produces a potential bis(1,2-dithienyl-dithiolene)nickel complex intermediate. (ii) Thienyl pyrolysis: The decomposition temperature of the two thienyl groups shows a similar trend, being highest for the longest chain substituent (NiTh16) and decreasing for the shorter chains (NiTh12 at 462 °C, NiTh8 at 450 °C, and NiTh4 at 382 °C). (iii) Final residue: The residue at 800 °C is likely a (dithiolene)nickel structure for NiTh8, NiTh12, and NiTh16, but it degrades to nickel sulfide for NiTh4. This analysis clearly demonstrates that the complexes with higher molecular weights (NiTh12 and NiTh16) exhibit higher decomposition temperatures for both the alkyl and thienyl groups, which strongly indicates an enhancement in the thermal stability resulting from the increased molecular weight. Fourier-transform infrared spectroscopy (FTIR) analysis yielded characteristic peaks at 2846 cm^{-1} and 2918 cm^{-1}, which are attributed to the stretching vibrations of the C—H bonds within the alkyl chains (Fig. 1c). A band at 3076 cm^{-1} is assigned to the stretching vibrations of the C—H bond within the ethenyl group. These results are consistent with the successful substitution of alkyl chains and thiophene groups on the target organonitrile complex.

For the photophysical properties of NiThR derivatives, their UV–vis-NIR absorption spectra were recorded in dichloromethane (10 μM) at room temperature, as shown in Fig. 1d. All complexes exhibit strong absorption within the 800–1200 nm region. Specifically, the maximum absorption wavelengths were determined to be 1054 nm for NiTh4, 1044 nm for NiTh8, 1041 nm for NiTh12, and 1040 nm for NiTh16, respectively, attributed to intervalence charge transfer (IVCT) transitions within the delocalized bis(dithiolene) ligand system. [34] Additionally, these molecules display visible absorption bands arising from ligand-to-metal charge transfer and intense π-π* transitions. In contrast, the fluorescence in the solutions of all complexes was observed to be dim, even quenching (Fig. S5). This quenching indicates that the

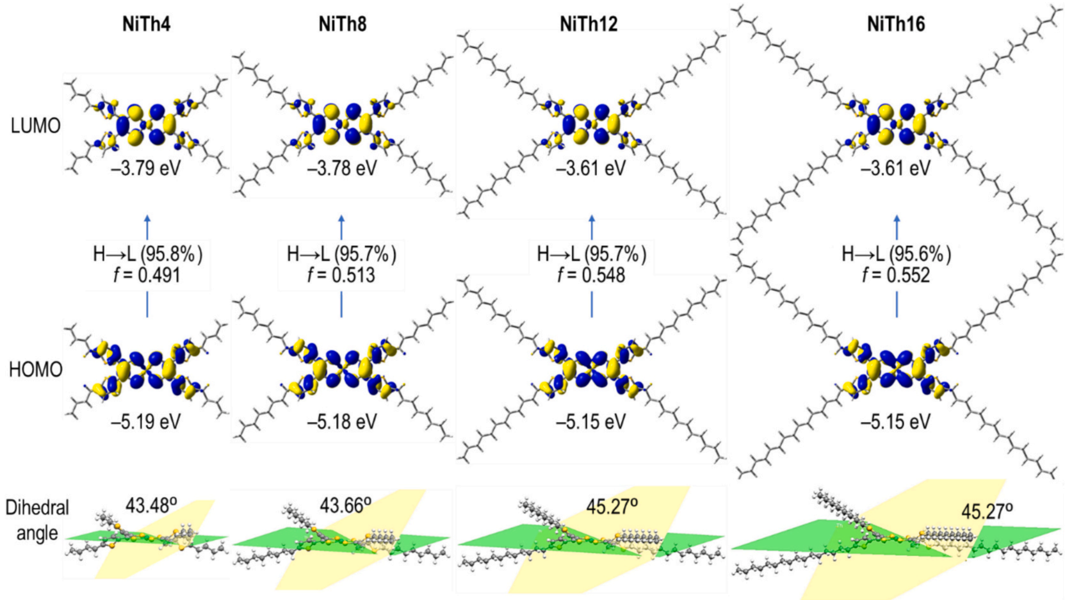

Fig. 2. Theoretical calculations of NiThR derivatives. Molecular orbitals with isovaluce of 0.02 au and energy levels of the highest occupied molecular orbital (HOMO) and the lowest unoccupied molecular orbital (LUMO), respectively, and their dihedral angles between the bis(dithiolene) nickel center (green plane) and thiophene (yellow plane), calculated with TD-DFT at the level of PBE1PBE/6-31G(d)/LANL2DZ. The *f* denotes the oscillator strength of the first transition. (For interpretation of the references to colour in this figure legend, the reader is referred to the web version of this article.)

excited molecules primarily dissipate energy through nonradiative internal conversion processes, resulting in the generation of heat rather than radiative emission. [35] To further explore their photothermal conversion behaviors, complexes in chlorobenzene (55 μg mL^{-1}) were irradiated with a 1064 nm laser (1 W cm^{-2}) for 10 min, and their temperatures (T_{Max}) were up to 56.4 °C (NiTh4), 58.7 °C (NiTh8), 58.0 °C (NiTh12), and 64.7 °C (NiTh16), respectively (Fig. 1e). After closing laser irradiation, the system time constants for heat transfer (τ_s) were fitted using the time-dependent temperature drop curve, yielding values of 64.5 s (NiTh4), 59.7 s (NiTh8), 50.0 s (NiTh12), and 50.2 s (NiTh16), respectively (Fig. 1f). The photothermal conversion efficiencies (PTCEs) [36] are further estimated to be 6.9%, 12.1%, 14.5%, and 30.1% for NiTh4, NiTh8, NiTh12, and NiTh16, respectively. Herein, NiTh16 achieves the highest PTCE primarily due to its significantly high temperature change ($\Delta T \sim 35.2$ °C) and its low time constant (τ_s) for heat transfer. Its low τ_s value indicates a more rapid change in the system's temperature in response to the driving force, translating to more efficient heat localization. This is achieved despite having the lowest effective absorption at 1064 nm (A_{1064}; Fig. S6) of the conjugation unit (the Ni-thienyldithiolene center). This result highlights that the efficient confinement and utilization of thermal energy (high ΔT and low τ_s) can be achieved by modifying the material with long alkyl chains, further enhancing its PTCE performance. Unfortunately, we must also note that target complexes with alkyl chains longer than C16 (n-hexadecyl-) are unable to form due to the requirements of the coordination reaction condition (in a hydrophilic environment). Moreover, according to the intramolecular motions restriction mechanism, nonradiative energy decay for the long alkyl chain substituted complex may be attributed to its active intramolecular motions. [37] This means that developing improved synthetic routes to obtain and study organometallic complexes with longer alkyl chains is a crucial strategy for fully optimizing the PTCE through intramolecular motions and heat localization, thereby fully realizing the potential of these materials in high-efficiency solar applications.

3.2. Theoretical calculations of NiThR derivatives

Time-dependent density functional theory, using the PBE1PBE functional and a 6-31G(d)/LANL2DZ basis set, was employed to calculate the NiThR derivatives and gain a detailed understanding of the photophysical mechanism. For the optimized molecular geometries (Fig. 2), the square-planar organonickel bis(dithiolene) complex is bound to thiophene, and the dihedral angles of NiTh4, NiTh8, NiTh12, and NiTh16 are 43.5°, 43.7°, 45.3°, and 45.3°, respectively. The smaller dihedral angles for NiTh4 and NiTh8 facilitate the delocalization of electrons from the thienyl ring to the organonickel complex, resulting in a downward shift in the energy levels of the highest occupied molecular orbital (HOMO) and the lowest unoccupied molecular orbital (LUMO). In contrast, NiTh12 and NiTh16 with long alkyl chain substituents have larger dihedral angles and energy gaps. For the same reason, as the alkyl chain lengthens, the first transition energy rises from 1.21 eV (NiTh4) to 1.34 eV (NiTh16), corresponding to the hypsochromic shift of the IVCT band, which is consistent with the UV–vis-NIR absorption data (Fig. 1c). In addition, according to the iMIPT mechanism [27], the large dihedral angle between the organonickel coordination center and thienyl ring planes leads to relatively loose intermolecular stacking, providing sufficient space for intramolecular motions in the aggregation state. Therefore, the configurational reorganization of NiTh16 with a long alkyl chain is relatively active during the de-excitation process compared with the other complexes. The nonradiative molecular relaxation of the former is more conducive to achieving higher photothermal conversion characteristics, which corresponds with the experimental results (Fig. 1d). Overall, from the perspective of theoretical calculations, alkyl chain engineering on organonickel complexes can enhance their solar light-harvesting capabilities and photothermal properties, promoting them to serve as the STCM for the SDIE evaporator.

3.3. The morphologies and SDIE performances of STILs based on NiThR derivatives

For SDIE fabrications, 3.0 mg of NiThR derivative adsorbed on filter paper (NiThR@FP) with a diameter of 18 mm was prepared as STILs. According to the different alkyl chain lengths, the filter paper (FP) substrates adsorbed with organonickel complexes are named NiTh4@FP (*n*-butyl-), NiTh8@FP (*n*-octyl-), NiTh12@FP (*n*-dodecyl-), and

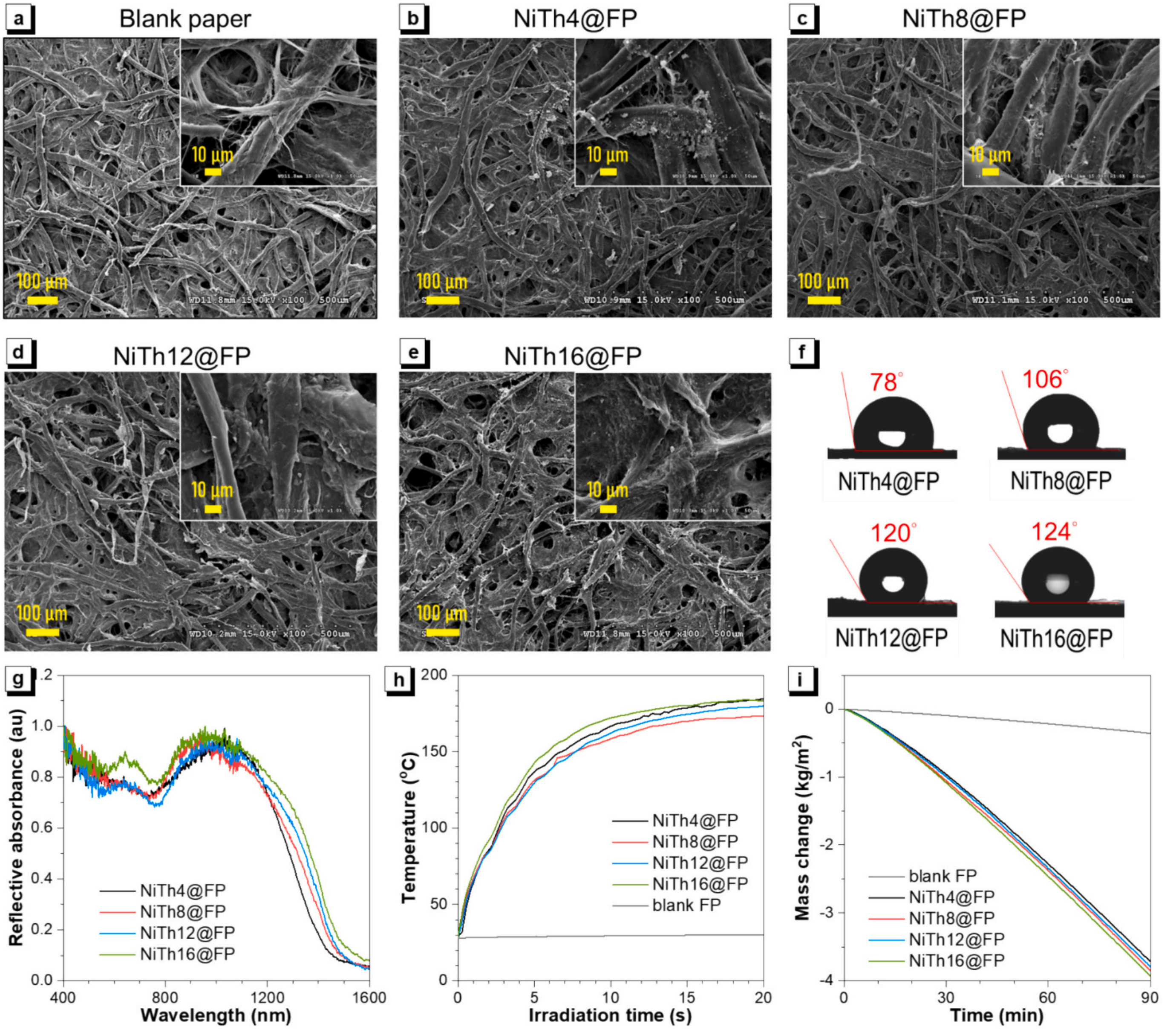

Fig. 3. The surface morphologies and solar-driven interfacial evaporation (SDIE) of NiThR derivatives-adsorbed filter papers (FPs). (a–e) Scanning electron microscope (SEM) images of (a) blank filter paper (FP), (b) NiTh4-, (c) NiTh8-, (d) NiTh12-, and (e) NiTh16-adsorbed filter papers. (f) The contact angle analysis, (g) the reflective UV–vis-NIR absorption spectra, (h) time-dependent temperature changes under 1064 nm irradiation (1 W cm^{-2}), and (i) water-mass change curves under one sun irradiation (1 kW m^{-2}) for 3 mg of NiThR-adsorbed filter papers, compared with blank FP.

NiTh16@FP (*n*-hexadecyl-). Insight into the structure revealed by SEM (Fig. 3a-e) shows that the surface of NiTh16-adsorbed filter paper (NiTh16@FP) is notably coarser than that of the blank one (Fig. 3a). This rougher surface indicates that the material adheres well to the paper fibers, and the ideal pore structure enhances the effective collection of sunlight within the filter paper, facilitating efficient water evaporation.[25] In contrast, the agglomeration and uneven distribution of complexes on the filter papers (Fig. 3b-d) can be observed using shorter alkyl chain-substituted complexes, which adsorb onto them. The fibers that are partially free of adsorbed complexes remain hydrophilic on the surface of filter papers. Therefore, with shortening alkyl chain length, the water contact angles (WCAs) of NiThR@FPs' surfaces decrease in the order of NiTh16, NiTh12, NiTh8, and NiTh4 (Fig. 3f), whereas their WCA values are almost zero as NiThR@FPs are wet (Fig. S7), i.e., during SDIE operation. Interestingly, the complex-adsorbed filter paper, in its final configuration, functions as a Janus structure evaporator. Herein, two distinct functional layers: (i) Hydrophobic top layer (photothermal surface) is functionalized with the organonickel complex and serves as the photothermal evaporator surface. It features a significantly large water contact angle (124°), confirming its hydrophobic nature (Fig. S8). This layer is responsible for efficient photothermal conversion and crucial anti-salt accumulation behavior, both of which are necessary for stable SDIE operation. (ii) Hydrophilic bottom layer (water transport), composed of the original filter paper cellulose, remains highly hydrophilic, exhibiting a low water contact angle (23°) (Fig. S8). This property ensures the continuous water supply to the top evaporative layer by efficiently drawing water up from a reservoir via capillary action. This result strongly suggests that utilizing organonickel complexes (due to their strong light absorption) on filter paper creates highly functional Janus evaporators, paving the way for efficient solar-powered desalination applications.

Furthermore, comparing the solution and solid-state absorption spectra of the complexes (Fig. S9), NiThR@FPs used as STILs in the SDIE system exhibit broad absorptions in the range of 400 to 1600 nm

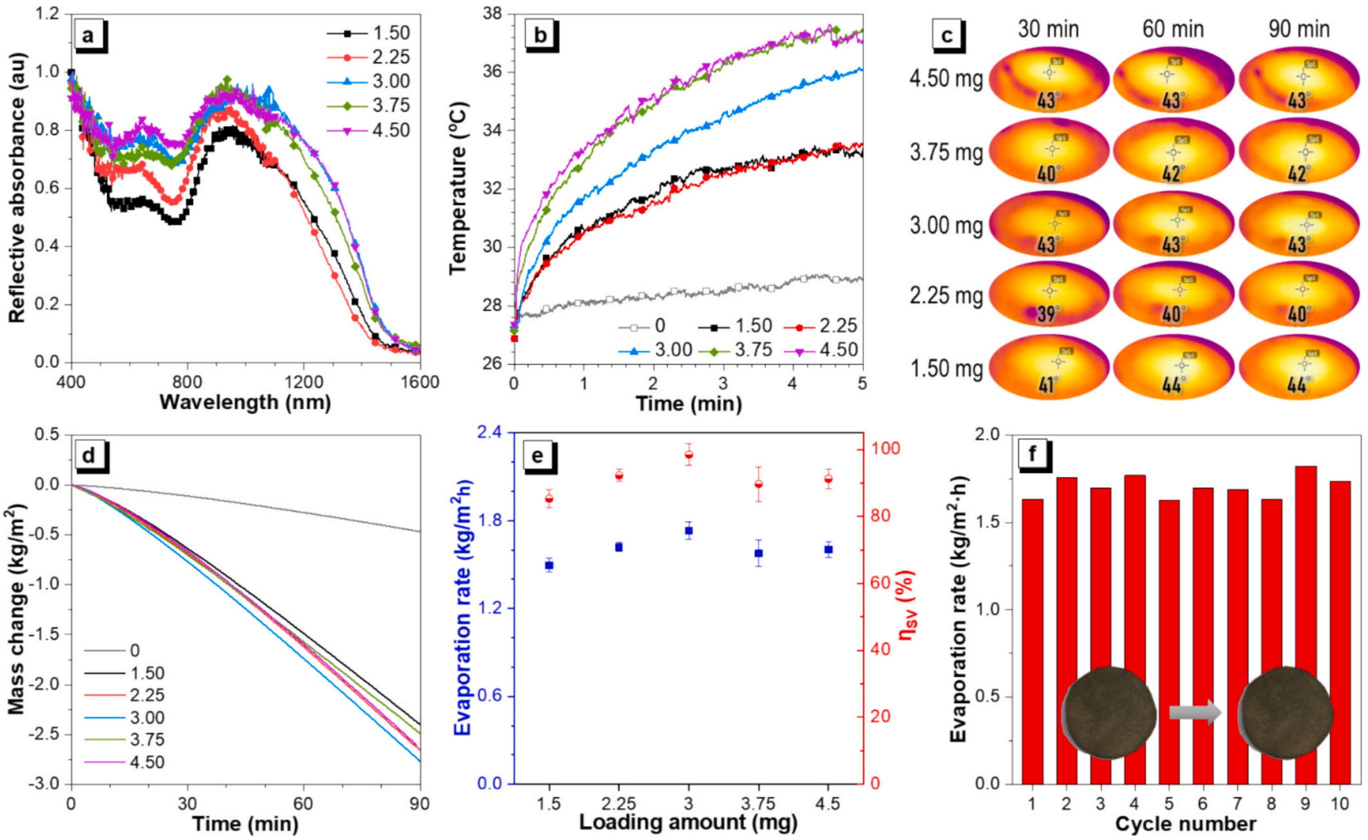

Fig. 4. SDIE performances of NiTh16@FP with different loading. (a) The reflective UV–vis-NIR absorption spectra of NiTh16@FP with different loading amounts of NiTh16 (1.50, 2.25, 3.00, 3.75, and 4.50 mg). (b) Time-dependent temperature changes and (c) infrared images of the solar-thermal interfacial-heating evaporation layers under one sun irradiation (1 kW m^{-2}). (d) Water-mass change curves and (e) the relationship between evaporation rate (blue) and solar energy-to-vapor efficiency (η; red) for different amounts of NiTh16-loading FPs under one sun irradiation. (f) SDIE stability for 3.0 mg of NiTh16-loading device. The inset of (f) is the surface change of NiTh@FP before and after SDIE work. (For interpretation of the references to colour in this figure legend, the reader is referred to the web version of this article.)

(Fig. 3g). This results from the close packing of complexes in the solid state, leading to coexisting π-π* transition and charge-transfer pathways that are responsible for the broad spectrum spanning the visible to NIR region [38]: (i) The π-π* transition is attributed to electronic coupling between neighboring complexes through π–π stacking and S⋯S orbital overlap, which mainly promotes visible absorption. (ii) Intermolecular intervalence charge transfer (IVCT) results from electronic coupling between neighboring Ni centers and π-conjugated dithiolene ligands. (iii) Intramolecular IVCT is the inherent charge transfer within a single molecule. The last two factors mainly contribute to enhanced near-infrared absorption. Therefore, the coexistence of these pathways creates an extended delocalization network, which in turn gives rise to the broad, continuous absorption band observed on the NiThR@FP. On the other hand, the difference in the absorption spectra between the NiThR@DC and NiThR@FP suggests distinct aggregation mechanisms. Specifically, the hypochromic shift in the maximum intervalence charge transfer (IVCT) wavelength is indicative of H-aggregate formation. In contrast, the bathochromic, broader absorption peak originates from intermolecular J-aggregation on the filter fiber.

These stacks not only effectively boost sunlight absorption rates but also suppress the radiative process and enhance the nonradiative heat release; thereby, the photothermal conversion temperatures of NiThR@FPs' surfaces rise to 173.4–184.6 °C over 20 s (Fig. 3h) under 1064 nm laser irradiation (1 W cm^{-2}), while the blank paper reaches only 30.0 °C. Interestingly, NiTh16@FP has the largest red-shifted absorption range compared with the others, which can be attributed to the uniform adsorption on the fiber surface (Fig. 3e) after modification with long alkyl chains. Hence, under one solar irradiation (1 kW m^{-2}), the deionized water evaporation rates ($\dot{m}$) of STILs based on NiTh4 (2.19 ± 0.10 kg m^{-2} h^{-1}), NiTh8 (2.25 ± 0.08 kg m^{-2} h^{-1}), NiTh12 (2.27 ± 0.06 kg m^{-2} h^{-1}), and NiTh16 (2.47 ± 0.02 kg m^{-2} h^{-1}) increase in sequence (Fig. 3i). Compared to the blank filter paper-based SDIE system (only 0.20 ± 0.01 kg m^{-2} h^{-1} of $\dot{m}$ value), the organonickel complex-modified STILs significantly accelerate water evaporation. The estimated solar energy-to-vapor efficiency (η_V) exceeds 100% of the theoretical value, owing to the porous morphology of NiThR@FP's surface (Fig. 3b-e), which efficiently captures incident solar irradiance and reduces reflection losses. [39] Despite this, the NiTh16-coated filter paper exhibits superior water evaporation performance compared to the other complex-adsorbed layers tested. Subsequently, NiTh16@FP will be investigated stepwise as the STIL for solar-driven water evaporation.

3.4. SDIE performances of NiTh16@FP

To evaluate the optimal dose of the complex on STIL, different amounts of NiTh16 (1.50, 2.25, 3.00, 3.75, and 4.50 mg) were loaded on a scaled-up filter paper with a diameter of 25 mm to fabricate NiTh16@FP STILs. For the reflective UV–vis-NIR absorption spectrum (Fig. 4a), the absorbance of NiTh16@FP reaches its highest when the complex loading exceeds 3.0 mg. Using a high quantity (4.5 mg) only slightly increases visible light absorption. Under one-sun illumination, the initial heating rate of NiTh16@FP STILs through photothermal conversion increases with the complex dose (Fig. 4b), while the final temperature reaches 40–44 °C within 90 min (Fig. 4c). The SDIE system reaches the maximum evaporation rate ($\dot{m}$) with the increase of complex dose from 1.5 mg (1.50 ± 0.04 kg m^{-2} h^{-1}) and 2.25 mg (1.62 ± 0.03

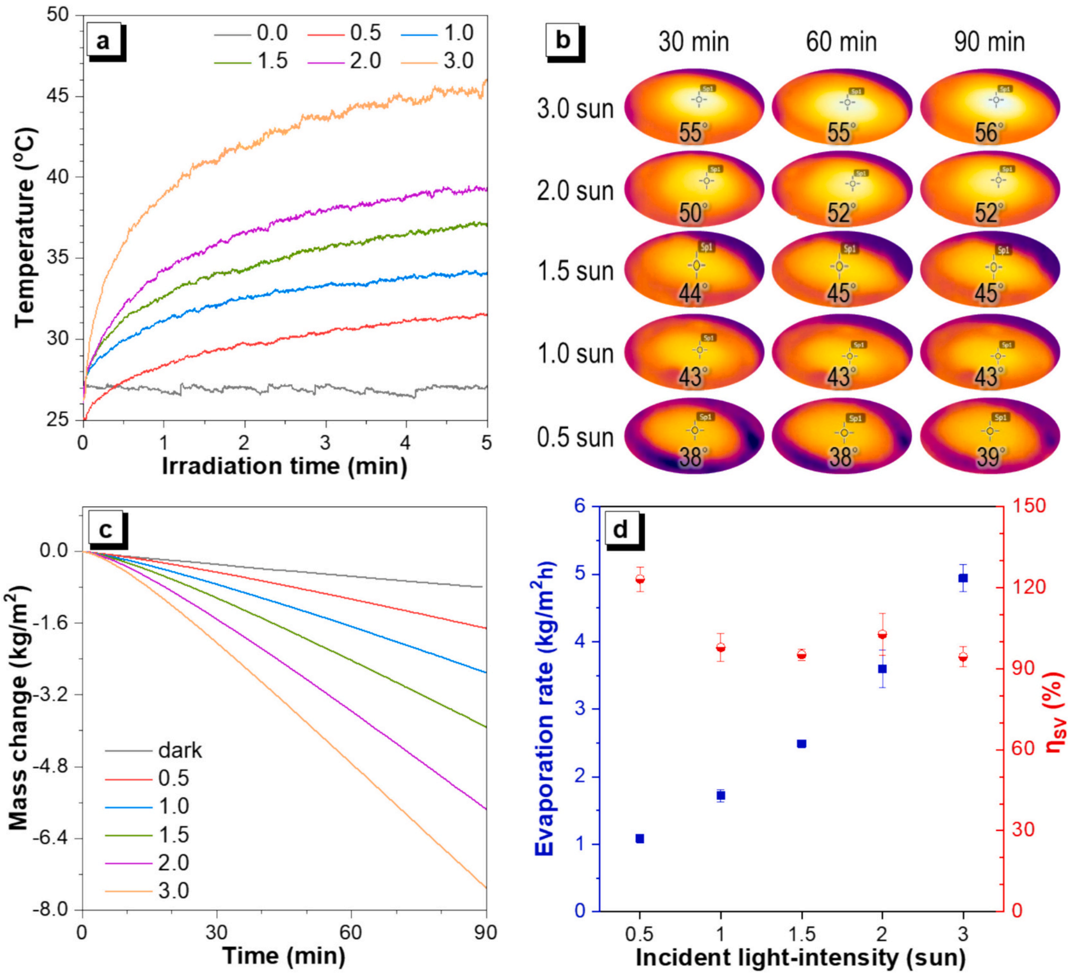

Fig. 5. SDIE performance of NiTh16@FP under different irradiation powers. (a) Time-dependent temperature changes, (b) infrared images of the solar-thermal interfacial-heating evaporation layers, (c) water-mass change curves, and (d) the relationship between evaporation rate (blue) and solar energy-to-vapor efficiency (η; red) for 3.0 mg of NiTh16-loading FPs under different irradiation powers (0.5–3 suns). (For interpretation of the references to colour in this figure legend, the reader is referred to the web version of this article.)

kg m^{-2} h^{-1}) to 3.0 mg (1.72 ± 0.09 kg m^{-2} h^{-1}), where the blank filter paper without complex adsorption exhibits only 0.28 kg m^{-2} h^{-1} of $\dot{m}$ value (Fig. 4d and e). By comparison, high complex-adsorbed evaporators display dropping $\dot{m}$ values of 1.58 ± 0.09 kg m^{-2} h^{-1} for 3.75 mg and 1.60 ± 0.05 kg m^{-2} h^{-1} for 4.50 mg, respectively. To analyze the surface morphology of evaporators using SEM (Figs. S10-S13), the pores were almost reduced or blocked with high dosage loading (Figs. S12 and S13), resulting in reduced performance. This indicates that the NiTh16@FP layer loaded with 3.0 mg is the optimal condition for solar energy-to-vapor generation, with an efficiency of 98.48 ± 3.27%. The efficiency exceeding 100% is likely a result of the light-trapping effect inherent to the evaporator's porous structure. Specifically, the pores of the NiTh16@FP material enhance the absorption of incident solar irradiance, minimizing reflection losses [40]. Thereafter, for 10 cycles of evaporated experiments, even though the evaporation rate fluctuates slightly, the $\dot{m}$ values and surface morphology do not change significantly (Fig. 4f), confirming the reusability and stability of NiTh16@FP for SDIE operation.

The SDIE device loaded with 3.0 mg NiTh16 was further irradiated at different power densities (0, 0.5, 1.0, 1.5, 2.0, and 3.0 suns) to observe the effect of light source intensity. As the sunlight intensity strengthens from 0 to 3.0 suns, the photothermal conversion temperatures increase sequentially (Fig. 5a). After being illuminated for 90 min, the surface temperature can rise to 56 °C using 3.0-solar radiation (Fig. 5b), whereas it changes only 0.6 °C in the dark. The deionized water's $\dot{m}$ values of SDIE devices also reveal an increasing tendency from 1.08 ± 0.04 kg m^{-2} h^{-1} at 0.5 sun, 1.72 ± 0.09 kg m^{-2} h^{-1} at 1 sun, 2.49 ± 0.06 kg m^{-2} h^{-1} at 1.5 suns, and 3.59 ± 0.28 kg m^{-2} h^{-1} at 2 suns to 4.94 ± 0.20 kg m^{-2} h^{-1} at 3 suns of illumination (Fig. 5c and d). Considering natural evaporation in the absence of solar illumination, the $\dot{m}$ value of the SDIE device in darkness was measured to be 0.56 kg m^{-2} h^{-1}, which is the inherent evaporation rate for all devices during operation. Furthermore, the observed linear increase in the evaporation rate with higher optical concentration, rather than an exponential trend, underscores the NiTh16@FP's ability to effectively manage the heat generated under intensified solar irradiance levels while maintaining robust structural stability.

3.5. Solar-powered desalination and outdoor evaporation test

Stability and durability are important characteristics because they determine the service life of the evaporator and, thus, the cost of the freshwater. Here, real seawater from the Sizihwan seawater (Kaohsiung, Taiwan) was used to investigate the stability and durability of the desalination evaporator over 10 cycles of use. As shown in Fig. 6a and b, the SEM images of the STIL surface without salt accumulation after multiple uses confirm the excellent salt-rejecting property of the as-prepared NiTh16@FP evaporator. This feature effectively prevents sunlight reflection and reduces conversion efficiency caused by salt deposition. Therefore, the water evaporation rate (1.67 ± 0.06 kg m^{-2}

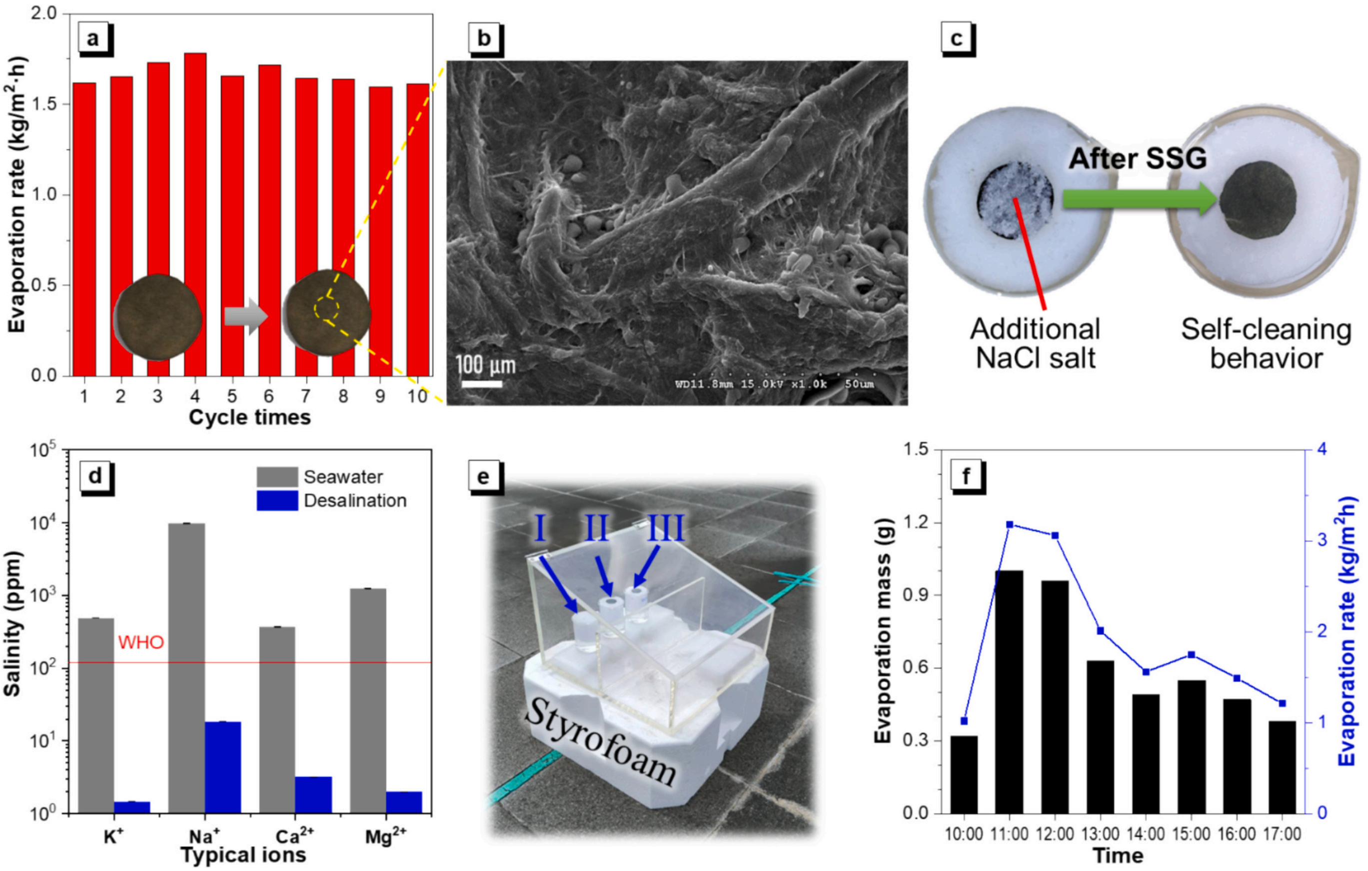

Fig. 6. Desalination application of NiTh16@FP. (a) The cycle solar energy-to-evaporation of 3.0 mg of NiTh16-loading SDIE device for Sizihwan seawater under 1 sun irradiation. The inset pictures are the surface of NiTh16@FP before and after desalination. (b) SEM images of the surface morphology of NiTh16@FP after desalination. (c) The self-cleaning test of NiTh16@FP. (d) Four ion concentrations of the seawater before and after desalination. (e) The outdoor solar-driven interfacial evaporation device (I: deionized water with blank FP; II: deionized water with NiTh16@FP; III: seawater with NiTh16@FP). (f) The outdoor water evaporation mass and rate with seawater of NiTh16@FP at different times.

h^{-1}) and the conversion efficiency (94.97%) remained unchanged during the entire measurement time (Fig. 6a). To further demonstrate the evaporator's ability to resist salt accumulation, a dynamic salt diffusion test was performed, where 0.8 g of NaCl salt was directly spread on the NiTh16@FP's surface (Fig. 6c). During the SDIE operation, the solar-driven capillary effect promotes an upward water flux, creating a vertical salt concentration gradient. This gradient facilitates salinity exchange via immediate diffusion, allowing the additional carpeted salt to be diluted and continuously transported back into the bulk brine solution [41], thus enabling self-cleaning. Furthermore, thanks to the hydrophobicity of the organonickel complex (Fig. 3f), its solar-absorbing evaporation layer prohibits salt deposition. [42] The combined effect ensures that NaCl salt rapidly dissolves into the photothermal film and eventually disappears on the STIL surface. This phenomenon showcases the self-cleaning capacity of the evaporator, facilitating the conversion of solar energy from seawater into vapor. Herein, the ion concentrations of the seawater, both before and after desalination, were assessed using inductively coupled plasma optical emission spectroscopy (ICP-OES) for accurate monitoring of salinity ion concentrations. The Sizihwan seawater initially contains 489.1 ppm of K^+, 9724 ppm of Na^+, 370 ppm of Ca^{2+}, and 1257 ppm of Mg^{2+} (Fig. 6d). Subsequent to SDIE evaporation, it is evident that the concentrations of four primary ions (1.48 ppm of K^+, 18.47 ppm of Na^+, 3.20 ppm of Ca^{2+}, and 2.00 ppm of Mg^{2+}) significantly decrease in the produced freshwater. These reduced levels are well below the World Health Organization (WHO) standards for safe drinking water ion concentrations [43].

Additionally, an outdoor evaporation test was conducted between 10:00 and 17:00 on August 8, 2025, on the rooftop of NKUST. The sunlight intensity reaches its highest at 12:00 (0.87 kW m^{-2}) and then decreases with time (Fig. S14). The maximum water evaporation rate for seawater in a NiTh16@FP-based device (Fig. 6e) is 3.18 kg m^{-2} h^{-1} at 11:00, and the solar irradiance is 0.71 kW m^{-2}. In comparison, the blank filter paper evaporator shows only 0.76 kg m^{-2} h^{-1} at 11:00 and 12:00 (Fig. S15). This indicates that the SDIE device with NiTh16@FP evaporator exhibits excellent performance for outdoor seawater desalination.

3.6. Solar-powered evaporation with sewage

To demonstrate the effectiveness of the water purification system in removing pollutants, wastewater samples simulating organic wastewater containing dye solutions, methyl blue (MB), methyl orange (MO), Rhodamine B (RhB), and methylene blue (MeB), were selected in this experiment. As shown in Fig. S16, UV–vis absorption spectra show that dye concentrations in the condensed water after treatment are close to zero, where the clarity of the solution is visible to the naked eye (the left of Fig. 7a–d). The $\dot{m}$ values based on pollution solutions are estimated to be approximately 1.65–1.69 kg m^{-2} h^{-1} (Fig. 7e). Moreover, regardless of whether the source water is acidic or alkaline, the pH value of the purified water remains stable at approximately 7 (Fig. 7f and g). These findings highlight the capability of NiTh16@FP-based solar water purification systems to efficiently purify a diverse range of water types in an environmentally friendly manner. Finally, considering fabrication costs, the estimated cost of a large-area NiTh16@FP evaporator is approximately $ 0.50 per square meter (Table S2). While the material's development cost is competitive with organic photothermal conversion materials [21,44] and low-cost inorganic or carbide-based SDIE systems.

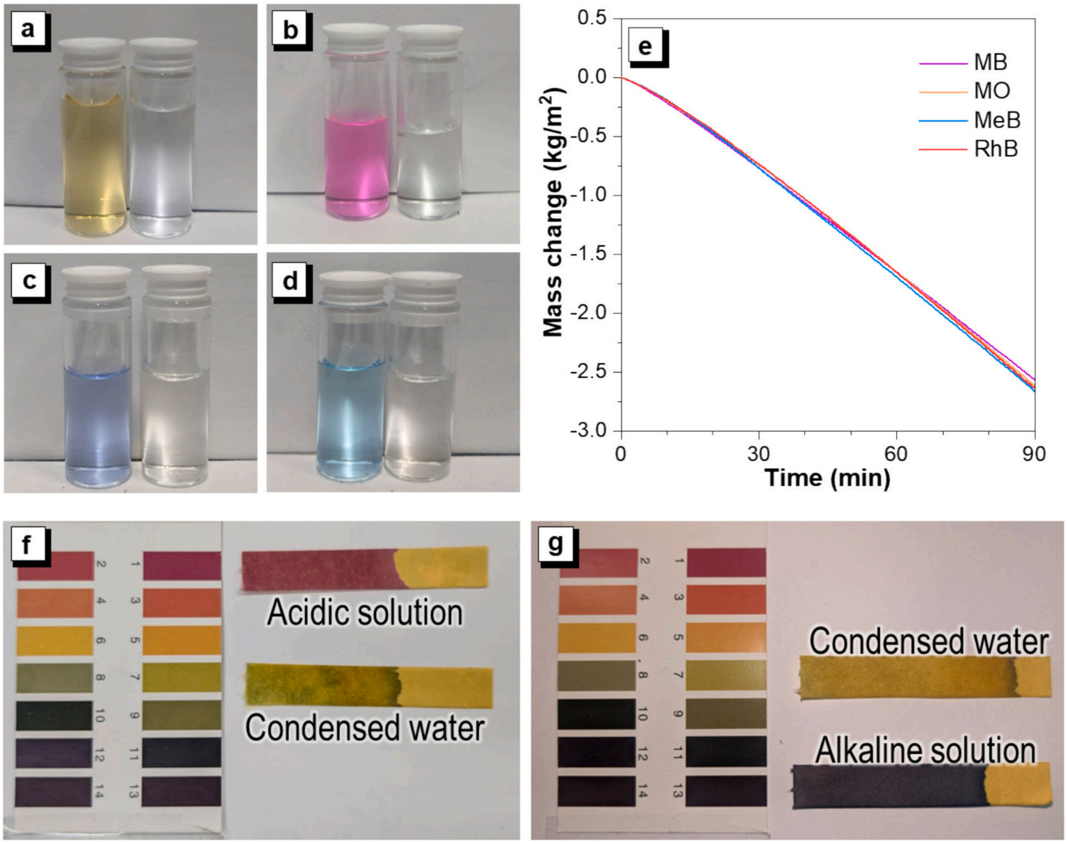

Fig. 7. SDIE application based on NiTh16@FP for wastewater. (a–d) Photographs of methyl orange (MO) (a), rhodamine B (RB) (b), methylene blue (ME) (c), and methyl blue (MB) (d) solutions and corresponding condensed water and (e) their water-mass change curves under one-sun irradiation. (f, g) The pH values before and after the purification of acidic (f) and alkaline (g) solutions. (For interpretation of the references to colour in this figure legend, the reader is referred to the web version of this article.)

[17,45,46] To achieve commercial viability, future efforts will focus on both improving synthesis efficiency to reduce material costs and enhancing cost-effectiveness by integrating multifunctional properties, such as photodynamic, thermoelectric, or anti-adhesion capabilities.

4. Conclusion

This study has developed a high-performance solar-driven interfacial evaporation system by integrating alkyl-chain-engineered organonickel bis(dithiolene) complexes onto a low-cost filter paper substrate. By extending the alkyl chain of the complex from n-butyl chains to n-hexadecyl chains, its thermal stability (182.3 and 321.7 °C of T_d for NiTh4 and NiTh16, respectively), photothermal conversion efficiency (6.9% for NiTh4 and 30.1% for NiTh16), absorption range, and adsorption behavior on the substrate were noticeably improved. The optimized evaporator based on NiTh16 photothermal material achieves evaporation rates of 1.72 ± 0.09 and 1.67 ± 0.06 kg m^{-2} h^{-1} for deionized water and seawater, respectively, under 1-sun irradiation, and also exhibits excellent cycling stability and desalination capability. For outdoor applications, the maximum water evaporation rate of 3.18 kg m^{-2} h^{-1} can be achieved at 11:00. These findings highlight the power of molecular design in tailoring organometallic photothermal agents and demonstrate the feasibility of combining such tunable complexes with water transport substrates for sustainable water purification. This work opens up new opportunities for the rational design of photothermal materials through terminal alkyl chain engineering, laying a foundation for the future development of next-generation multifunctional SDIE systems.

CRediT authorship contribution statement

Joanna S. Lin: Writing – original draft, Methodology, Formal analysis, Data curation, Conceptualization. **Pei-Yu Chen:** Methodology, Formal analysis, Data curation. **Chen-Yang Hsu:** Investigation, Formal analysis, Data curation. **Chen-Chieh Ni:** Writing – original draft, Visualization, Methodology. **Xinggui Gu:** Writing – review & editing, Visualization. **Jen-Shyang Ni:** Writing – review & editing, Visualization, Supervision, Project administration, Funding acquisition, Conceptualization.

Declaration of competing interest

The authors declare the following financial interests/personal relationships which may be considered as potential competing interests: Jen-Shyang Ni reports financial support was provided by National Science and technology council (Taiwan). If there are other authors, they declare that they have no known competing financial interests or personal relationships that could have appeared to influence the work reported in this paper.

Acknowledgments

We are grateful for financial support from the National Science and Technology Council (NSTC 114-2113-M-992-001, Taiwan) and computational and storage resource support from the National Center for High-Performance Computing (NCHC, Taiwan), a part of the National Applied Research Laboratories (NARLabs, Taiwan).

Appendix A. Supplementary data

Supplementary data to this article can be found online at https://doi.org/10.1016/j.seppur.2025.136139.

Data availability

Data will be made available on request.

References

[1] N.M.A. Omar, M.H.D. Othman, Z.S. Tai, M.F. Rabuni, A.O.A. Amhamed, M. H. Puteh, J. Jaafar, M.A. Rahman, T.A. Kurniawan, Overcoming challenges in water purification by nanocomposite ceramic membranes: a review of limitations and technical solutions, J. Water Process Eng. 57 (2024) 104613.

[2] L. Huang, L. Ding, J. Caro, H. Wang, MXene-based membranes for drinking water production, Angew. Chem. Int. Ed. 62 (2023) e202311138.

[3] T.M. Joseph, H.E. Al-Hazmi, B. Sniatala, A. Esmaeili, S. Habibzadeh, Nanoparticles and nanofiltration for wastewater treatment: from polluted to fresh water, Environ. Res. 238 (2023) 117114.

[4] W. Shang, T. Deng, Solar steam generation: steam by thermal concentration, Nat. Energy 1 (2016) 16133.

[5] Y. Xiao, H. Guo, M. Li, J. He, X. Xu, S. Liu, L. Wang, T.D. James, Strategies for enhancing the photothermal conversion efficiency of solar-driven interfacial evaporation, Coord. Chem. Rev. 527 (2025) 216378.

[6] M. Rengasamy, N. Eswaramoorthy, A. Gnanasekaran, K.G.G.N.S.S.S.M.S. K. Rajaram, Optimization of 3D-printed solar evaporators for enhanced interfacial solar steam generation and beyond: investigating surface modifications and nanocomposite coatings, Mater. Today Sustain. 26 (2024) 100816.

[7] H.W. Lim, S.H. Park, S.J. Lee, 3D thermoresponsive hydrogel with enhanced water uptake and active evaporation for effective interfacial solar steam generation, Desalination 550 (2023) 116368.

[8] M.S. Asghar, M.S. Irshad, N. Arshad, M. Al Huwayz, M. Alomar, G. Maqsood, M. A. Ali, M. Sabir, S. Xie, N.X. Ho, V.-D. Dao, X. Wang, J. Li, Z. Guo, 3D solar evaporator with conical alumina concentrator for efficient desalination and wastewater treatment, Sep. Purif. Technol. 380 (2026) 135326.

[9] M. Rousta, A. Kia, A. Kasaeian, Application of nanomaterials as photo-thermal agents in solar desalination: a review of experimental approaches, Desalination 598 (2025) 118379.

[10] Y. Wang, Y. Liao, P. Wang, Y. Zhang, Y. Li, Recent development and improvements of cotton fabric-based solar-driven interfacial evaporators: a review, Desalination 607 (2025) 118795.

[11] G. Tian, C. Duan, B. Zhao, K. Yang, J. Guo, Y. Wen, B. Zhou, J. Wang, Y. Ni, Janus structured cellulose-based aerogel with vertical channels and conical roof for efficient solar-driven water evaporation and pollutant degradation, Carbohydr. Polym. 360 (2025) 123622.

[12] M.J. Margeson, M. Atwood, Y.E. Monfared, M. Dasog, Plasmonic group 4 transition metal carbide interfaces for solar-driven desalination, Aggregate 5 (2024) e531.

[13] N. Zhou, Z. Fan, I. Noh, Y. Wang, B. Li, H.D. Kim, B. Xiao, Q. Zhou, H. Ohkita, B. Wang, Versatile polyimide composite aerogels for highly efficient interfacial solar steam generation through controlling the molecular polarity, Sep. Purif. Technol. 378 (2025) 134539.

[14] Y. Lin, W. Han, E. Xu, H. Wang, Y.-T. Pan, K. Yao, J. Gong, High performance of interfacial solar-driven water evaporation and power generation by ZIF-8 derived N-doped porous carbon polyhedron, Sep. Purif. Technol. 377 (2025) 134227.

[15] C. Ma, W. Wang, Q. Chen, R. Zhang, R. Yan, Z. Jia, X. Zhang, W. Zhang, L. Wang, C. Wang, Repurposing facial tissue waste to construct flexible hierarchical MOF-based photothermal material with lower evaporation enthalpy for high efficient solar-driven seawater desalination and wastewater purification, Desalination 600 (2025) 118472.

[16] S. Zeng, J. Si, Z. Cui, Z. Yuan, Metal-organic framework-based materials for solar-driven interfacial evaporation, Chem. Eng. J. 502 (2024) 158111.

[17] X. Mu, W. Han, H. Zhang, R. Li, C. Bai, W. Li, Y. Xie, Y. Liu, All-in-one MXene/PDA@MF-EF solar steam generator with semi-clad construction for efficient interfacial evaporation, water purification and desalination, Sep. Purif. Technol. 361 (2025) 131344.

[18] Y. Song, X. Hu, M. Wang, J. Bai, S. Ma, S. Tong, Calla lily-inspired 3D evaporator: a dual interface design for enhanced solar water evaporation, Desalination 597 (2025) 118361.

[19] S.-F. Pan, W.-X. Xia, W.-L. Feng, L. Ma, S.-J. Ding, X.-B. Chen, Enhanced photothermal conversion in ReS_2/Bi_2Se_3 nanoflowers for solar-driven thermoelectric power generation and water evaporation, J. Alloys Compd. 1020 (2025) 179390.

[20] M. Wang, C.Y. Lin, Y. Sagara, T. Michinobu, Enhanced photothermal property of NDI-based conjugated polymers by copolymerization with a thiadiazolobenzotriazole unit, ACS Mater. Au 4 (2024) 82–91.

[21] J.C. Yang, L. Wu, L. Wang, R. Ren, P. Chen, C. Qi, H.T. Feng, B.Z. Tang, An efficient photothermal conversion material based on D-A type luminophore for solar-driven desalination, Aggregate 5 (2024) e535.

[22] Y. Khakre, S.C. Marinescu, Electronic structure and mechanistic understanding of electrochemical H_2 evolving activity of metal-bis(dithiolenes), Coord. Chem. Rev. 535 (2025) 216586.

[23] M.D. Roy, T.P. Gompa, S.M. Greer, N. Jiang, L.S. Nassar, A. Steiner, J. Bacsa, B. W. Stein, H.S. La Pierre, Intervalence charge transfer in nonbonding, mixed-valence, homobimetallic ytterbium complexes, J. Am. Chem. Soc. 146 (2024) 5560–5568.

[24] Y.-T. Lin, J.S. Lin, Y.-C. Yang, J.-S. Ni, Organonickel complex J-aggregation on interfacial evaporator promotes broadband absorption and salt rejection for efficient solar-powered desalination, Desalination 593 (2025) 118201.

[25] Y.-C. Yang, J.S. Lin, J.-S. Ni, Neutral d^8 metal complexes with intervalence charge-transfer transition trigger an effective NIR-II photothermal conversion for solar-driven desalination, J. Mater. Chem. A 11 (2023) 26164–26172.

[26] A. Velusamy, S. Yau, C.L. Liu, Y. Ezhumalai, P. Kumaresan, M.C. Chen, Recent studies on small molecular and polymeric hole-transporting materials for high-performance perovskite solar cells, J. Chin. Chem. Soc. 70 (2023) 2046–2063.

[27] M.-C. Chen, Y.-J. Chiang, C. Kim, Y.-J. Guo, S.-Y. Chen, Y.-J. Liang, Y.-W. Huang, T.-S. Hu, G.-H. Lee, A. Facchetti, T.J. Marks, One-pot [1+1+1] synthesis of dithieno[2,3-*b*:3′,2′-*d*]thiophene (DTT) and their functionalized derivatives for organic thin-film transistors, Chem. Commun. (2009) 1846–1848.

[28] Y. Liang, Y. Pan, L. Chen, P. Li, M. Xu, H. Zhou, X. Lu, W. Hu, C. Yin, Q. Fan, Alkyl-doping enables significant suppression of conformational relaxation and intermolecular nonradiative decay for improved near-infrared fluorescence imaging, Angew. Chem. Int. Ed. 63 (2024) e202408861.

[29] J.-S. Ni, X. Zhang, G. Yang, T. Kang, X. Lin, M. Zha, Y. Li, L. Wang, K. Li, A photoinduced nonadiabatic decay-guided molecular motor triggers effective photothermal conversion for cancer therapy, Angew. Chem. Int. Ed. 59 (2020) 11298–11302.

[30] X. Duan, Q. Zhang, Y. Jiang, X. Wu, X. Yue, Y. Geng, J. Shen, D. Ding, Semiconducting polymer nanoparticles with intramolecular motion-induced photothermy for tumor phototheranostics and tooth root canal therapy, Adv. Mater. 34 (2022) e2200179.

[31] Z. Zhao, C. Chen, W. Wu, F. Wang, L. Du, X. Zhang, Y. Xiong, X. He, Y. Cai, R.T. K. Kwok, J.W.Y. Lam, X. Gao, P. Sun, D.L. Phillips, D. Ding, B.Z. Tang, Highly efficient photothermal nanoagent achieved by harvesting energy via excited-state intramolecular motion within nanoparticles, Nat. Commun. 10 (2019) 768.

[32] M. Alaasar, A.F. Darweesh, Y. Cao, K. Iakoubovskii, M. Yoshio, Electric field- and light-responsive oxadiazole bent-core polycatenar liquid crystals, J. Mater. Chem. C 12 (2024) 1523–1532.

[33] W. Wei, X. Zhou, S. Pang, J. Zhou, X. Yuan, J. Li, Y. Chen, L. Pan, Z. Xie, H. Wu, F. Huang, Y. Cao, C. Duan, A–D–A'–D–A type nonfused ring electron acceptors for efficient organic solar cells via synergistic molecular packing and orientation control, Aggregate 5 (2024) e488.

[34] B. Mogesa, E. Perera, H.M. Rhoda, J.K. Gibson, J. Oomens, G. Berden, M.J. van Stipdonk, V.N. Nemykin, P. Basu, Solution, solid, and gas phase studies on a nickel dithiolene system: spectator metal and reactor ligand, Inorg. Chem. 54 (2015) 7703–7716.

[35] J.-S. Ni, G.-H. Lu, Natural protoberberine alkaloid-montmorillonite nanocomposite powders with AIE features for visualizing high-resolution latent fingerprints, Spectrochim. Acta A Mol. Biomol. Spectrosc. 300 (2023) 122908.

[36] J.-B. Pluta, N. Bellec, F. Camerel, Investigation of the photothermal properties of a large series of metal-bis(dithiolene) complexes: impact of the molecular structure and ranking using the photothermal index I_{PT}, Dyes Pigments 226 (2024) 112130.

[37] Y. Li, Y.-X. Wang, D. Liu, C.-C. Ni, J. Ni, J.-S. Ni, Structural isomerism engineering regulates molecular AIE behavior and application in visualizing endogenous hydrogen sulfide, J. Mater. Chem. B 12 (2024) 11134–11141.

[38] R. Kato, Conducting metal dithiolene complexes: structural and electronic properties, Chem. Rev. 104 (2004) 5319–5346.

[39] T. Jiang, S. Bian, Y. Wang, X. Fan, L. Zhu, X. Song, G. Wang, T. Wang, H. Zhang, The nexus of solar absorption and morphology designs based on 2D photothermal materials: from rational design to advanced application of water purification, Chem. Eng. J. 499 (2024) 156450.

[40] A.M. Saleque, M.N.A.S. Ivan, S. Ahmed, Y.H. Tsang, Light-trapping texture bio-hydrogel with anti-biofouling and antibacterial properties for efficient solar desalination, Chem. Eng. J. 458 (2023) 141430.

[41] R.T. Ginting, H. Abdullah, D.A. Barus, V. Fauzia, Extremely high-efficiency solar steam generation, robust and scalable photothermal evaporator based on ZIF-67@MXene/rGO decorated rock wool, J. Mater. Chem. A 11 (2023) 5296–5308.

[42] X. Yu, Q. Zhang, X. Liu, N. Xu, L. Zhou, Salt-resistive photothermal materials and microstructures for interfacial solar desalination, Front. Energy Res. 9 (2021) 721407.

[43] R.K. Mahajan, T.P. Walia, B.S. Lark, Sumanjit, analysis of physical and chemical parameters of bottled drinking water, Int. J. Environ. Health Res. 16 (2006) 89–98.

[44] L. Sun, H. Wu, Z. Zhang, K. Wu, J. Sun, X. Dong, C. Dong, C. Zhao, X. Gu, D.H. Qu, A smart visualized phototherapy switch: from NIR-I imaging-guided photodynamic therapy to NIR-II-guided photothermal therapy for enhanced cascade tumor photoablation, Aggregate 6 (2025) e70007.

[45] Y. Hu, J. Xu, Y. Chen, F. Pei, J. Lu, J. Yan, W. Cheng, D. Wang, L. Bai, G. Han, Y. Zhang, Lotus-inspired cellulose-based aerogel with Janus wettability and vertically aligned vessels for salt-rejecting solar seawater purification, Carbohydr. Polym. 352 (2025) 123158.

[46] H. Lian, R. Ding, Z. Liu, Q. Yan, H. Chen, Y. Chen, T. Fei, J. Xiong, H. Zheng, F. Xue, X. Zhao, Q. Peng, X. He, A sunflower-inspired nonwoven fabric evaporator for autonomous phototropic tracking and continuous efficient evaporation under sunlight, Chem. Eng. J. 514 (2025) 163312.